Vessel and Intracranial Aneurysm Segmentation Using Multi-range Filters and Local Variances

Max W.K. Law and Albert C.S. Chung

Lo Kwee-Seong Medical Image Analysis Laboratory,
Department of Computer Science and Engineering,
The Hong Kong University of Science and Technology, Hong Kong
{maxlawwk,achung}@cse.ust.hk

Abstract. Segmentation of vessels and brain aneurysms on non-invasive and flow-sensitive phase contrast magnetic resonance angiographic (PCMRA) images is essential in the detection of vascular diseases, in particular, intracranial aneurysms. In this paper, we devise a novel method based on multi-range filters and local variances to perform segmentation of vessels and intracranial aneurysms on PCMRA images. The proposed method is validated and compared using a synthetic and numerical image volume and four clinical cases. It is experimentally shown that the proposed method is capable of segmenting vessels and aneurysms with various sizes on PCMRA images.

1   Introduction

Brain aneurysms are vascular diseases caused by abnormal dilation of the cerebral arteries. The presence of brain aneurysms is potentially fatal as the burst of aneurysms can lead to severe internal bleeding. In the past decade, there has been a growing interest in the detection of brain vessels and aneurysms by performing analysis on angiography. Hernandez *et al.* proposed two training based geodesic active region methods in [1,2], and a technique using the Hessian matrix [3] and a Gaussian mixture model in [4] to segment aneurysms in computed tomography (CT) angiography. Kawata *et al.* made use of a template that a sphere was attached on a tube to discover aneurysms based on cone-beam CT images. In [5], Bruijne *et al.* described how to perform segmentation of aneurysms in multi-spectral magnetic resonance images with the help of user interaction when training data was limited.

As a non-invasive and flow-sensitive acquisition technique, phase contrast magnetic resonance angiographic (PCMRA) images are useful to assess patient conditions. One of the limitations of the PCMRA images is the low image contrast of vasculature, especially the regions inside aneurysms. Furthermore, due to slow blood flow inside aneurysms, the intensity values of aneurysms are significantly lower than those of the vessels in PCMRA. The intensity drops between vessels and the attached aneurysms create large intensity changes which are easy to be misinterpreted as vessel boundaries and cause incorrect segmentation of aneurysms by the traditional vascular segmentation approaches such as [6,7].

In this paper, a novel method is proposed for the segmentation of intracranial aneurysms in PCMRA images. The proposed method requires neither training,

which causes the segmentation results depending on the training data; nor shape assumption, which is possibly inflexible to handle variation of aneurysm shapes. To cope with the aforementioned limitations of PCMRA images, the proposed method makes use of a new detection filter and local variances. This detection filter aims at recognizing the intensity changes of the aneurysm boundaries. This filter complements with local variances to reduce the effect of noise and suppress the responses induced from high intensity vessels to avoid the missing of low intensity aneurysms. Furthermore, a multi-range scheme is employed to provide a detection response to handle the size variations of aneurysms. The proposed method is validated and compared using a synthetic and numeric image volume, and four PCMRA images acquired from a collaborating hospital. It is experimentally shown that the proposed method is capable of segmenting low contrast aneurysms with various sizes on PCMRA images.

2 Methodology

A New Detection Filter
To determine whether a local voxel is inside an aneurysm, it is necessary to detect the intensity changes induced by the aneurysm boundaries. Along a line from a voxel inside an aneurysm to any position of the image background, an intensity drop can be observed at the aneurysm boundary. The first part of this work is to devise a filter to detect such intensity changes. Due to the variations of sizes and shapes of aneurysms, this filter is required to be sensitive to the intensity changes that occur in different directions and distances relative to a local voxel in an aneurysm.

To design such a detection filter, a set of translated and rotated first derivative of Gaussian filters are added up as a single detection filter. To illustrate this idea, we firstly consider the filter in a 1D case, i.e. $f_{l,\sigma}^{1D}(x) = \frac{1}{2}(G_x^\sigma(x+l)+G_{-x}^\sigma(-x-l))$, where G_x^σ is the first derivative of a Gaussian function with the scale parameter σ along x. $f_{l,\sigma}^{1D}$ includes translating and differentiating the Gaussian function in both the x and $-x$ directions to detect intensity changes that occur in any direction in 1D (including the positive and negative directions) and distance l away from a local pixel (see Fig. 1a and Fig. 1c is in the case of 2D). In 3D cases, the filter is given by,

$$f_{l,\sigma}(x,y,z) = \frac{1}{K}\sum_{k}^{K} G_{\hat{n}_k}^\sigma(x+l\hat{n}_k\cdot(1,0,0)^T, y+l\hat{n}_k\cdot(0,1,0)^T, z+l\hat{n}_k\cdot(0,0,1)^T),$$

(1)

where $\hat{n}_k$ is the k-th orientation sample and K is the total number of the orientation samples which sweep across the surface of a sphere (see an example in Fig. 1d). In our implementation, the total number of orientation samples K guarantees that there is at least one orientation sample for each unit area on the surface of a sphere having radius l. This isotropic filter is capable of detecting intensity changes that take place in any direction with distance l away from a local voxel. As such, for a local voxel located in l voxels away from the aneurysm

boundary, the filtering response of this local voxel is negative if it is inside an aneurysm, or positive if it is outside an aneurysm.

Multi-Range Detection and Local Variances
Using the above detection filter, a multi-range scheme is employed to recognize intensity changes that occur in various distances away from a local voxel. The multi-range scheme is based on obtaining responses using a group of $f_{l,\sigma}$ with various values of l and a small constant value σ. The main purpose of utilizing various values of l instead of σ is that the enlargement of σ intends to anni-hilate low contrast structures. Based on the multi-range scheme, there are as many filtering responses as the number of ranges being utilized. However, for a range that does not match the distance between a local voxel and the aneurysm boundary, the corresponding filtering response is possibly driven by noise and becomes unreliable. It is essential to have another measurement to appropriately suppress the responses associated with undesired ranges prior to the employment of a multi-range scheme.

To suppress the responses of undesired ranges, local variances are utilized,

$$V_{l,\sigma}(x,y,z) = \int B_{l,\sigma}(u,v,w)\{I(x+u,y+v,z+w) - \mu_{l,\sigma}(x,y,z)\}^2 dudvdw, \quad (2)$$

where μ is the averaged intensity of the local region covered by $B_{l,\sigma}(x,y,z)$, $\mu_{l,\sigma}(x,y,z) = \int B_{l,\sigma}(u,v,w)I(x+u,y+v,z+w)dudvdw$, and $B_{l,\sigma}$ is a filter of smoothed spherical step function with radius $l+\sigma$, defined as,

$$B_{l,\sigma} = G^\sigma * b_{l+\sigma} \text{ where } b_r(x,y,z) = \begin{cases} 1/4\pi r^3 & \text{if } \sqrt{x^2+y^2+z^2} \le r \\ 0 & \text{otherwise.} \end{cases} \quad (3)$$

An 1D example of the above filter, denoted as $B_{l,\sigma}^{1D}$, is shown in Fig. 1b. This filter $B_{l,\sigma}$ is designed to cover a region that $f_{l,\sigma}$ is close to or equal to zero. The local variance $V_{l,\sigma}(x,y,z)$ based on this filter quantifies the local intensity similarity within the coverage of $B_{l,\sigma}$. It returns a large value if the intensity values inside the filter coverage are fluctuating. Such fluctuation implies that an object boundary passes though the filter coverage and thus, this local region possibly belongs to different objects. Therefore, the filtering response of $f_{l,\sigma} * I$ is unreliable for deciding whether a local voxel is inside an aneurysm. Hence, we weight the response $f_{l,\sigma} * I$ by the local variance $V_{l,\sigma}$ to acquire a reliable measure, which reflects how likely a local voxel is inside an aneurysm,

$$R_{l,\sigma}(x,y,z) = \frac{f_{l,\sigma} * I(x,y,z)}{\sqrt{V_{l,\sigma}(x,y,z)} + \rho}, \quad (4)$$

where ρ is a parameter which should be assigned with the consideration of the intensity values of the dimmest part of the target aneurysm. Since the coverage of the spherical filter $B_{l,\sigma}$ (Eq. 3) used by $V_{l,\sigma}$ includes the coverage of $f_{l,\sigma}$ (see Figs. 1a and b), the intensity changes which can be detected by $f_{l,\sigma}$ also affect the local variance $V_{l,\sigma}$. For a high contrast boundary, such as boundaries of vessels connected with aneurysms, it can result in a local variance value which
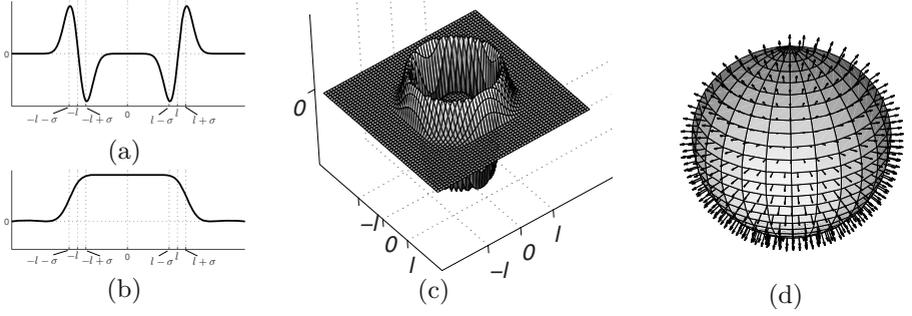
Fig. 1. (a) $f_{l,\sigma}^{1D}(x)$. (b) $B_{l,\sigma}^{1D}(x)$. (c) $f_{l,\sigma}^{2D}(x,y)$. (d) An example of orientation samples taken for computation of $f_{l,\sigma}^{3D}(x,y,z)$.

is large relative to ρ (i.e. $\sqrt{V_{l,\sigma}} >> \rho$). Weighting the filtering responses $f_{l,\sigma}$ by $\sqrt{V_{l,\sigma}} + \rho$ not only suppresses the responses obtained in undesired ranges, but also restrains the value of $R_{l,\sigma}$ from being too large with the presence of high contrast boundaries where both the values of $f_{l,\sigma} * I$ and $V_{l,\sigma}$ increase. It is beneficial to avoid the high contrast vessel boundaries dominating the detection results and causing missing of low intensity aneurysms in segmentation results.

Grounded on the detection response in Eq. 4, a set of detection ranges l, denoted as $L = \{l_1, l_2, ..., l_P\}, l_1 < l_2 < .... < l_P$, is used for multi-range detection,

$$S_{L,\sigma}(x,y,z) = \max\{R_{l_1,\sigma}(x,y,z), 0\} + \min\{\min_q(R_{l_q,\sigma}(x,y,z)), 0\}. \quad (5)$$

The minimum range, l_1 should be assigned with the consideration of the narrowest part of the aneurysm. The rest of the ranges in L are suggested to ensure that the voxels inside the aneurysm can reach the aneurysm boundary by a distance included in L. $S_{L,\sigma}$ in Eq. 5 embodies two components, the former part is positive valued, which determines if a local voxel is outside an aneurysm away from the boundary of the aneurysm with distance l_1. It is zero if $R_{l_1,\sigma}(x,y,z)$ is negative which indicates that in the range l_1, the voxel is located inside an aneurysm. For the later component, it is negative valued and judges how likely a local voxel is inside an aneurysm. It searches all ranges for the highest negative detection response which indicates that the local voxel is inside an aneurysm.

Active Surface Model
The multi-range detection response described above is able to indicate how likely a voxel belongs to an aneurysm (negative responses) or outside an aneurysm (non-negative responses). Based on this detection response, a level set framework [8] is utilized to find a region which maximizes the negative multi-range detection response. As such, a level set function ψ is evolved as $\frac{d\psi}{dt} = S|\nabla\psi| + \kappa\left(\nabla\frac{\nabla\psi}{|\nabla\psi|}\right)$, where κ is a length regularization term which is 0.05 in our implementation to maintain surface smoothness. The other parameters to solve the differential equation follow the description in [9] and the implementation is based on [10].

The evolution of the level set function is stopped when the accumulated per-voxel update of the level set function was less than 10^{-5} for 10 iterations.

3   Experimental Results

A synthetic and numerical volume and four clinical PCMRA images were utilized in the experiments. Two gradient based active surface segmentation methods (Geodesic Active Contour, **GAC** [6]; Flux Maximizing Geometric Flows, **FLUX** [7]) were implemented and compared with the proposed method (**MRFLV**). In **FLUX** and **GAC**, all the images involved were pre-smoothed by a Gaussian with the scale parameter 1. In **GAC**, an edge detector $1/(1 + |m\nabla I_\sigma|^n)$ was employed, where I_σ was the smoothed image, $n = 4$ and $n = 2$ for the synthetic and clinical volumes respectively; $m = 32$ and $m = 1$ for synthetic and clinical volumes respectively to enlarge the intensity changes of edges for the edge detector so that the object boundaries can be located correctly. The above parameters were set carefully to provide the best segmentation results for **GAC** in the experiments. For **MRFLV**, σ was 1 (Eq. 4) in all the experiments. Other parameters such as the radii associated with the multiscale scheme of **FLUX**, the range set L (Eq.5) and ρ (Eq.4) of **MRFLV** were assigned according to the conditions of images based on the description presented in Section 2. The values of those parameters are indicated individually in the figure captions for different cases, Figs. 3, 4, 5.

A synthetic and numerical image volume
In the first experiment, a synthetic and numerical image volume was used (Fig. 2). In this volume, a tube was attached with eight spheres with various combinations of sizes and intensities (Figs. 2a and b). This volume was smoothed

(a)   (b)   (c)
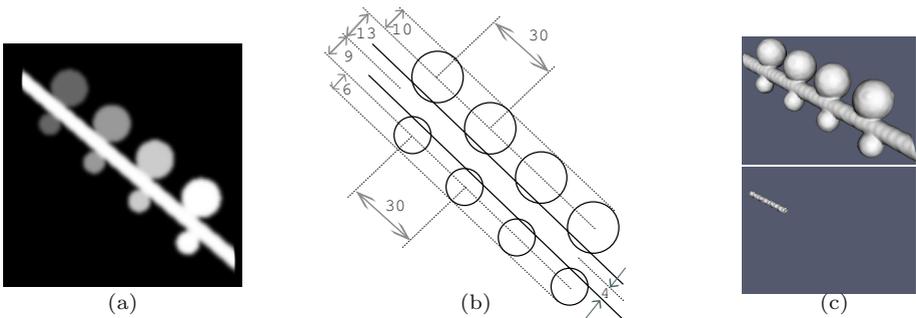
Fig. 2. The $128 \times 128 \times 128$ voxel synthetic and numerical image volume. (a) A maximum intensity projection of the image volume. From the upper left corner to the lower right corner, the intensity values for each pair of spheres with radii 10 and 6 voxels are 0.4, 0.6, 0.8 and 1.0 respectively. (b) The description of the settings of the image volume, the numbers are in unit voxel. (c) Top: The isosurface of the image volume. Bottom: The initial level set function utilized in the experiments.
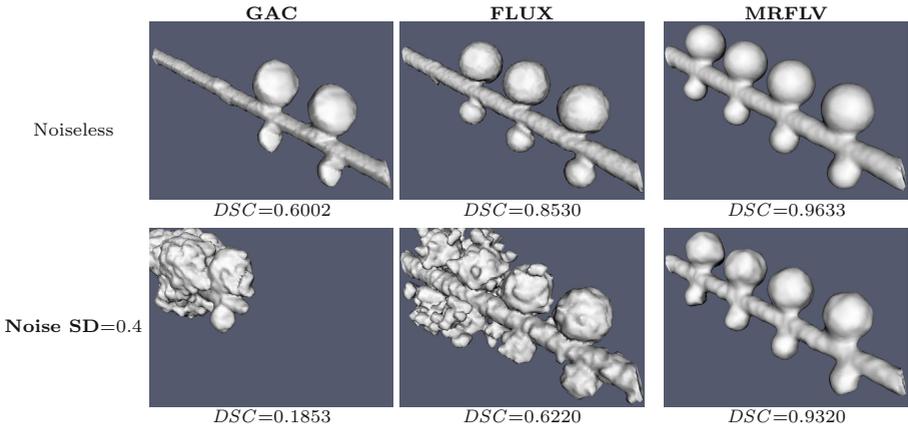
Fig. 3. The segmentation results of **GAC**; **FLUX**, radii={2, 3...6}; and **MRFLV**, $\rho = 4, L = \{2, 3...6\}$
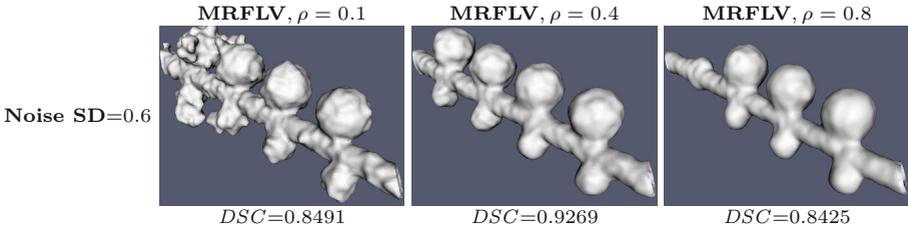
Fig. 4. Segmentation results of **MRFLV**, $L = \{2, 3...6\}$ various values of ρ

with a Gaussian filter ($\sigma = 1$) to mimic the smooth intensity transition between different structures. In addition, Rayleigh noise with different noise levels (specified by standard deviation and mentioned as **Noise SD** hereafter) was utilized to corrupt the image. The noise levels, **Noise SD**s, were assigned according to the fact that the image background intensity standard deviation is similar to the intensity of aneurysms in the clinical cases. There are two challenges to segment all spheres attached on the tube without leakage. First, the high intensity changes occurred at the connection between the tube and the low intensity spheres prohibit the active surface to propagate into the low intensity spheres. Second, the low contrast boundaries of the low intensity spheres result in inadequate intensity changes to stop the evolution of surface and lead to leakages.

   MRFLV, **FLUX** and **GAC** were applied on the noiseless and **Noise SD**=0.4 cases with the initial level set function shown in the bottom of Fig. 2c. In Fig. 3, the segmentation results and Dice Similarity Coefficient (DSC) [11] are shown. In the noiseless case (first row of Fig. 3), both **GAC** and **FLUX** were not able to pick all the spheres as the surfaces were halted by the high intensity changes of the connections between the low intensity spheres and the tube. For the noisy case (second row of Fig. 3), **GAC** and **FLUX** had leakages. It is worth

to mention that leakages or unfaithful halts of surfaces lead to unsatisfactory performance of aneurysm segmentation. On the contrary, **MRFLV** (Fig. 3) that was able to pick all the spheres without leakage in the both cases is suitable to discover low intensity aneurysms attached to high intensity vessels.

For **Noise SD**=0.6, only **MRFLV** was examined as other methods were failed when **Noise SD**=0.4. This case demonstrated the results of **MRFLV** using various values of ρ (Eq. 4). As stated previously, the value of ρ should be assigned with the intensity value of the dimmest part of the target aneurysm. An undersized ρ resulted in high sensitivity of low contrast voxels which leads to leakage (left of Fig. 4). On the other hand, a large value of ρ causes missing of low contrast structures (right of Fig. 4). With properly assigned values of ρ, $\rho = 0.4$, **MRFLV** provided the best results (middle of Fig. 4). Furthermore, the slight drop of DSC values of **MRFLV** between different noisy cases and the noiseless case (the third column of Fig. 3 and middle of Fig. 4) implies that **MRFLV** is robust to handle noisy cases. Such robustness is essential to prevent leakages when performing segmentation of low intensity aneurysms.

Clinical cases

In the clinical cases, to demonstrate the results of **MRFLV**, the slices of the aneurysmal regions and the resultant contours of **MRFLV** are shown in Fig. 5. Since the voxel intensity inside aneurysms are significantly lower than the vessels which the aneurysms attached on, to display the aneurysms along with the vessels, the pixels having intensity larger than 350 are displayed as having intensity value 350. Due to the space limitation, the result comparison is focused on the regions containing aneurysms. The cases that no observable result was obtained due to severe leakages at the position of aneurysms are indicated as "Failed". The initial seeds for these four cases were obtained by thresholding the 0.2% of the total number of voxels with the highest intensity values.

The segmentation results of these clinical cases are presented in Fig. 5. It is observed that **GAC** has leakages and cannot segment the aneurysms in these cases (Figs. 5b, c, f, g, j and l. Also, **FLUX** has leakage in the first case (Figs. 5b and c). The main cause of leakages is that the evolving surfaces followed the noise attached on the aneurysm boundaries. Although **FLUX** had no leakage in the second, third and forth cases (Figs. 5f, g, j and l), **FLUX** could not discover the low intensity parts of the aneurysms (Figs. 5f, g, j and l). In contrast, **MRFLV** demonstrated a promising performance to cope with the aneurysms in different shapes (irregular shape in the first and second cases, Figs 5a-h; and blob shapes in the rest of the cases, Figs 5i-m) and various sizes (see the differences of the detection ranges utilized in the first, second cases in Figs. 5b, c, f, g and the third, forth cases in Figs. 5j and l). Furthermore, since the initial seeds were obtained by intensity thresholding and they were located in the high intensity major vessels, the active surfaces of **MRFLV** were able to evolve from the high intensity vessels to the low intensity aneurysms. As such, the proposed method is shown to be able to handle the intensity drops in the connection of the vessels and the aneurysms (see the contours in Figs 5d, h, k and m, and the vessel

Region size (voxel size)	Resultant surfaces			Source image & Contours	Source image
118 × 62 × 18 (0.4 × 0.4 × 1.0 mm³)	(a)	**MRFLV**, $L = \{0.8, 1.2, ..., 4\}$mm, $\rho = 80$ **FLUX**, radii= $\{0.8, 1.2, ..., 4\}$mm **GAC**	**Failed** (b) (c)	(d)	
236 × 190 × 18 (0.4 × 0.4 × 1.0 mm³)	(e)	**MRFLV**, $L = \{0.8, 1.2, ..., 4\}$mm, $\rho = 80$ **FLUX**, radii= $\{0.8, 1.2, ..., 4\}$mm **GAC**	(f) (g)	(h)	
174 × 186 × 27 (0.4 × 0.4 × 0.9 mm³)	(i)	**MRFLV**, $L = \{1.6, 2, ..., 12\}$mm, $\rho = 80$ **FLUX**, radii= $\{0.8, 1.2, ..., 12\}$mm **GAC**	**Failed** (j)	(k)	
152 × 198 × 42 (0.4 × 0.4 × 0.8 mm³)	**MRFLV**, $L = \{1.6, 2, ..., 8\}$mm, $\rho = 80$ **FLUX**,radii= $\{0.8, 1.2, ..., 8\}$mm **GAC**		(l)	(m)	
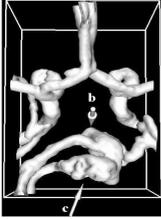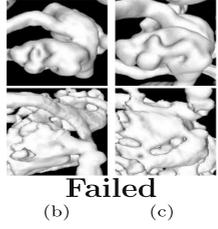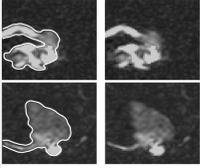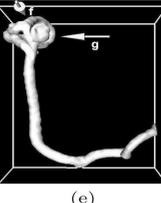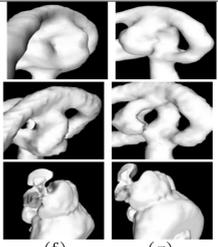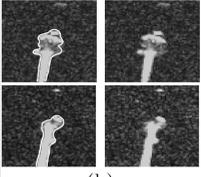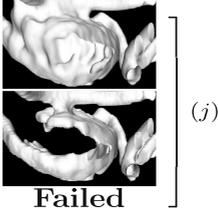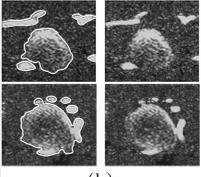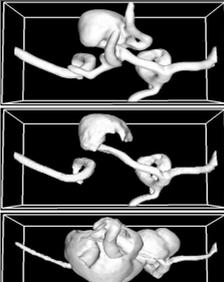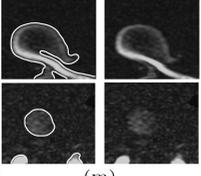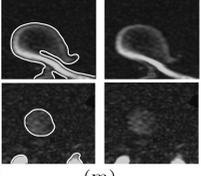
Fig. 5. The segmentation results of clinical cases corresponding to four regions of interest extracted from four distinct PCMRA images. (a-d) The first case; (e-h) the second case; (i-k) the third case; (l, m) the forth case. (a, e, i, l(top)) The resultant surfaces of **MRFLV** in the regions of interest. (a, e, i) The white arrows show the positions of the aneurysms and the view angles to obtain the zoomed-views shown in (b, c, f, g, j). (l(middle, bottom)) The resultant surfaces of different methods in the regions of interest. (b, c, f, g, j) The zoomed-views of the segmentation results of different methods at the aneurysm regions. (d, h, k, m) Slices of the aneurysmal regions and the corresponding contours of **MRFLV**, the pixels having intensity larger than 350 are shown as having intensity value 350 for the purpose of illustration.

intensities are higher than those appeared in these figures as the intensity above 350 were cropped for better visualization only).

4   Conclusion

We have presented a new method to segment vessels and intracranial aneurysms in PCMRA image volumes. The proposed method, called **MRFLV**, is validated using a synthetic and numerical image volume and four clinical cases. In the experiments, **MRFLV** is capable of selecting the low intensity aneurysms having various sizes and shapes without leakages of active surfaces, as well as coping with the intensity changes occurred in the connection between vessels and aneurysms. Two gradient based vascular segmentation approaches are utilized to compare with **MRFLV**. It is experimentally demonstrated that **MRFLV** can provide promising segmentation results of aneurysms on PCMRA images.

References

1. Hernandez, M., Frangi, A.: Geodesic active regions using non-parametric satistical regional description and their application to aneurysm segmentation from cta. In: MIAR, pp. 94–102 (2004)
2. Hernandez, M., Frangi, A., Sapiro, G.: Three-dimensional segmentation of brain aneurysms in cta using non-parametric region-based information and implicit deformable models: method and evaluation. In: Ellis, R.E., Peters, T.M. (eds.) MICCAI 2003. LNCS, vol. 2879, pp. 594–602. Springer, Heidelberg (2003)
3. Sato, Y., Nakajima, S., et al.: Three-dimensional multi-scale line filter for segmentation and visualization of curvilinear structures in medical images. MedIA. 2(2), 143–168 (1998)
4. Hernandez, M., Barrena, R., et al.: Pre-clincial evaluation of implicit deformable models for three-dimensional segmentation of brain aneurysms in cta. In: SPIE MI pp. 1264–1274 (2003)
5. Bruijne, M., Ginneken, B., et al.: Automated segmentation of abdominal aortic aneurysms in multi-spectral mr images. In: Ellis, R.E., Peters, T.M. (eds.) MICCAI 2003. LNCS, vol. 2879, pp. 538–545. Springer, Heidelberg (2003)
6. Caselles, V., Kimmel, R., Sapiro, G.: Geodesic Active Contours. ICCV 22, 61–79 (1997)
7. Vasilevskiy, A., Siddiqi, K.: Flux Maximizing Geometric Flows. T. PAMI. 24(12), 1565–1578 (2002)
8. Malladi, R., Sethian, J., Vemuri, B.: Shape Modeling with Front Propagation: A Level Set Approach. T. PAMI 17(2), 158–175 (1995)
9. Whitaker, R.: A Level-Set Approach to 3D Reconstruction from Range Data. IJCV 29(33), 203–231 (1998)
10. Ibanez, L., Schroeder, W., Ng, L., Cates, J. (The ITK Software ToolKit)
11. Zijdenbos, A., Dawant, B., et al.: Morphometric analysis of white matter lesions in mr images: Method and validation. IEEE. TMI 13(4), 716–724 (1994)